**Article:**
Ng, F.S.L. (2015) Spatial complexity of ice flow across the Antarctic Ice Sheet. Nature Geoscience, 8. 847 -850. ISSN: 1752-0894

https://doi.org/10.1038/ngeo2532

Post print (reviewed, pre-copy-edited version) of :

**Ng, F. S. L.** (2015) Spatial complexity of ice flow across the Antarctic Ice Sheet.

*Nature Geoscience*, 8(11), 847-850. doi:10.1038/ngeo2532

# Spatial complexity of ice flow across the Antarctic Ice Sheet

Felix S. L. Ng[1]

[1]*Department of Geography, University of Sheffield, Sheffield S10 2TN, UK*

**Fast-flowing ice streams carry ice from the interior of the Antarctic Ice Sheet toward the coast. Understanding how ice-stream tributaries operate and how networks of them evolve is essential for developing reliable models of the ice sheet's response to climate change[1–6]. A particular challenge is to unravel the spatial complexity of flow within and across tributary networks. Here I define a measure of planimetric flow convergence, which can be calculated from satellite measurements of the ice sheet's surface velocity, to explore this complexity. The convergence map of Antarctica clarifies how tributaries draw ice from its interior. The map also reveals curvilinear zones of convergence along lateral shear margins of streaming, and abundant ripples associated with nonlinear ice rheology and changes in bed topography and friction. Convergence on ice-stream tributaries and their feeding zones is uneven and interspersed with divergence. For individual drainage basins as well as the ice sheet as a whole, fast flow cannot converge or diverge as much as slow flow. I therefore deduce that flow in the ice-stream networks is subject to mechanical regulation that limits flow-orthonormal strain rates. These findings provide targets for ice-sheet simulations and motivate more research into the origin and dynamics of tributarization.**

Ice streams have been studied by geomorphological analysis of their surface and bed forms[7–9], radar and seismic imaging of their internal and basal properties[9-13], borehole measurements[14], and thermomechanical modelling[15–21]. Models can mimic ice-stream flow in numerical simulations[16–20] but are still probing the uncertain physics of basal-lubricated ice motion coupled with subglacial hydrology[16–18] and of shear-margin development and migration[21]. That subglacial geology can influence the location of ice streams, and major bed-topographic channels focus their flow, and in turn be shaped by it, is recognized[11,22]. But how networks of interacting ice-stream tributaries form, and what controls their dendritic (sometimes anastomosing) pattern, remain enigmas. Morphometric analysis of their flow field can shed light on these questions by uncovering order behind its complexity.

The essence of any non-uniform flow pattern is its directional variability. Tributarization of ice-sheet flow inherently involves flow merging and splitting, as evident from how flowlines converge/diverge, which is quantifiable as spatial rates of change of flow direction. To investigate this amorphous geometry, I propose a novel measure of planimetric flow convergence $C$, based on the surface ice-flow direction $\theta(X, Y)$ (measured clockwise from the $Y$-axis in radian; $X$ and $Y$ are horizontal coordinates), and compute a near-continuous visualization of $C$ across Antarctica. Away from singular points at saddles and summits[23], $\theta$ is continuous and differentiable. I define convergence as its rate of change across flow $C = \partial\theta/\partial n$, with $n$ pointing left-perpendicular to flow; thus $C > 0$, $< 0$ and $= 0$, respectively, if the flow is locally converging, diverging and parallel, whether or not it curves (Methods; Supplementary Fig. 1). Notice 'divergence' herein means $C < 0$, not divergence of a vector field; and $\partial\theta/\partial s$, where $s$ points along flow, quantifies flow curvature, not merging/splitting. Locally, $C$ equals the cross-flow compressive strain rate divided by flow speed $U$

50 (Methods) so it can sensitively detect convergence/divergence in slow flow. The *C*-
51 values reported below for ice streams fall within ± several $km^{-1}$, about four orders of
52 magnitude less than *C* for a kitchen drain vortex.

53 I derived the $\theta$-field from the Interferometric Synthetic Aperture Radar-
54 (INSAR-) based surface velocity map of Antarctica[6]. Then I computed *C* by a kriging
55 procedure, which treats $\theta$ as an intrinsic random field with auto-correlation properties
56 obeying its variogram (Supplementary Fig. 2) and evaluates *C* as a linearly-unbiased
57 estimate of the directional derivative of $\theta$, while suppressing effects of uncorrelated
58 noise in $\theta$ (Methods).

59 The convergence map (Fig. 1) bears an unmistakable imprint of ice-stream
60 networks and shows two distinct convergence textures (Figs 1b–f and 2) that broadly
61 occupy regions of different speeds. 'Chaos' texture, characterized by an intricate pattern
62 of intense convergence and divergence alternating over distances of several kilometres
63 or less, dominates the interior, mountains, ice rises and ridges, where $U \lesssim 20$ m $a^{-1}$. Its
64 convergence pattern is unreliable and neglected from analysis, because it inherits
65 abundant artefacts from the INSAR velocity and shows weak noise suppression
66 expected from the low flow speeds, which are comparable to errors in the INSAR
67 velocity measurements (a few to 17 m $a^{-1}$; ref. 6). 'Streaming' texture undulates gently
68 over longer distances and occurs on ice-stream tributaries/trunks, outlet glaciers and ice
69 shelves, where $U \gtrsim 20$ m $a^{-1}$. I call the respective regions 'chaos regions' and
70 'streaming regions'. Besides these textures, long curvilinear convergent or divergent
71 zones several kilometres wide commonly inhabit tributary/trunk shear margins and ice-
72 rise/ridge boundaries, reflecting strong lateral compression or extension where flank
73 flow joins streaming flow. Some convergent zones merge and extend downstream at
74 tributary confluences.

The map evidences rich structures in the switch from deformation-dominated slow flow to basal-slip dominated streaming flow, extending earlier inferences (from the velocity field)[6] that non-uniformities pervade ice-sheet flow. Notably, in slower-moving areas of streaming regions, where ice flow feeding and within ice-stream tributaries is expected to merge overall as it accelerates[13], convergence is markedly heterogeneous (e.g. where $20 \lesssim U \lesssim 200$ m a$^{-1}$ in Figs 1b–f). Here, sinuous ripples in $C$ of both signs are widespread, often with spacings of O(10) km and axes diagonal or sub-parallel to flow; some ripples grade into the fine-scale chaos. The faster flow on ice-stream and outlet-glacier trunks is smoother in texture, but not devoid of ripples.

Comparison of the convergence map with the ice sheet's basal topography from the BEDMAP2 dataset[24] confirms that some ripples—notably neighbouring pairs signed oppositely in $C$—record surface velocity perturbations associated with flow over subglacial peaks or ridges/steps[25] (Fig. 2; ellipses in Figs 1d,f). Ripples occurring far from shear margins where the bed appears smooth are likely caused by ice-rheological softening[26] (thus they may indicate failed or developing shear margins) or flow over sticky/slippery spots[25,27]. The latter possibility is supported by ice-flow modelling for Pine Island Glacier and Thwaites Glacier[28], which infers ribbed domains of high basal friction with similar spacing and orientation as ripples (Supplementary Fig. 3). Comparing the convergence in chaos regions with their bed roughness is not undertaken, because it is error-prone and much of the interior is poorly resolved by BEDMAP2[24].

Fundamental properties of Antarctic ice flow are revealed by the tower-shaped plot of speed $U$ against convergence $C$ (Fig. 3a). At each speed, $C$ ranges positive and negative far from the theoretical small divergence for a radially-spreading ice sheet ($C \approx -1/(60U)$ km$^{-1}$ for 3-km thick ice receiving 0.1 m a$^{-1}$ accumulation; Methods). This

bifurcation of $C$ is a hallmark of flow within tributary networks, which converges in some areas and diverges in others. Except at speeds $\gtrsim$ 2,000 m $a^{-1}$, where localized flow near ice-shelf edges and cracks causes a minor enhancement in convergence/divergence, the tower flanks indicate monotonic decay of the extreme values of $C$ with $U$, and a maximum speed for flow converging/diverging at each rate. Blank regions outside the tower reflect the absence of strongly converging/diverging fast flow.

Furthermore, the $C$-values at each speed are concentrated in a histogram peak much narrower than their range (well within ±0.2 $km^{-1}$; thus the colours in Figs 1 and 2b portray most $C$-values of streaming texture and saturate mainly extreme values of chaos texture), and the convergence and divergence at half-peak height, $C_+$ and $C_-$, decay with $U$ for $U \lesssim$ 2,000 m $a^{-1}$ (Figs 3c,d). These decays and the tower flanks in Fig. 3a imply that slow flow can converge and diverge more than fast flow across the grounded portion of the ice sheet. This macroscopic speed dependence of the $C$-value distribution holds regardless of the convergence in chaos regions and accords with: (1) observed relationships between convergence and velocity patterns (e.g. Fig. 2) and (2) the expectation that basal obstacles and sticky/slippery spots disturb fast flow less (bifurcate $C$ less) than slow flow. However, since this 'tower dependence' holds across different parts of the system (ice-stream trunks, tributaries, feeding zones, margins) and two orders of magnitude in $U$, it must have a more general mechanical origin than envisioned in (2)—as discussed shortly. The dependence is robust and universal. It is corroborated by increasing smoothness of the $\theta$-field with speed (Supplementary Fig. 2) and insensitive to rekriging with the flow-direction variogram of streaming regions (Supplementary Figs 4b–d). Tower-shaped plots are also found for individual drainage basins hosting different ice-stream networks (Fig. 3e). Although a spurious tower dependence could arise from corruption of $C$ in slower-flowing streaming regions by

INSAR-velocity errors, error analysis excludes this possibility (Methods; Supplementary Fig. 5). As is consistent with overall capture of ice into tributaries, the $C$-value distribution is asymmetric for $20 \lesssim U \lesssim 200$ m $a^{-1}$ (Figs 3a,c,d); in this range, which encompasses streaming onset and tributary feeding zones, the area of converging flow exceeds that of diverging flow by 12.2%; the mean convergence is +0.012 $km^{-1}$.

The tower dependence teaches us about the dynamics as well as latent geometry of tributarized flow. Since $C$ is flow-orthonormal compressive strain rate over $U$, the ubiquitous tower shape may be due primarily to this $1/U$-normalization (which enables conversion between geometry and deformation), modulated by flow-orthonormal strain rates. This interpretation is valid because the strain-rate distribution is weakly speed-dependent for $U \lesssim 2{,}000$ m $a^{-1}$ (Fig. 3b): at such speeds, the decay curves in Fig. 3c follow $U \propto |C_{\pm}|^{-1.4}$ approximately, so strain rates have the half-peak range $U|C_{\pm}| \propto U^{0.29}$. (The diffused tower flanks are harder to trace for curve fitting.) While these power laws indicate deviation of the tower dependence from $U \propto |C_{\pm}|^{-1}$ expected from the normalization, the critical discovery here is that the dependence occurs because flow-orthonormal strain rates at vastly different speeds have similar distributional widths, with half-peak range ~$10^{-2}$ $a^{-1}$ (Fig. 3b). This behaviour points to concerted mechanical regulation of the tributarized flow.

Deciphering the mechanisms behind the regulation is important for understanding the ice-stream networks because it underlies an entire hierarchy of tributarization structures. Indeed, any successful theory of the networks must explain the observed speed dependence of the distribution of $C$, or equivalently, of strain rate (as summarized by the power laws), which is a signature of their dynamical complexity. The mechanisms presumably involve ice rheology because non-zero $C$ implies

deformation; strain rates may be limited by internal feedbacks on ice viscosity, e.g. via its temperature and strain-rate controls or anisotropy, as occur at shear margins[15,21]. But local rheological descriptions (based on Glen's law) seem unable to predict the dependence directly, because they relate stress to strain rates (velocity gradients), not speed. The mechanisms must also involve the spatial connectedness of flow in the networks, because regulation acts on the surface strain-rate tensor resolved in a flow-related direction. Glaciological theories have yet to address such non-local aspect of ice streaming. The concept of flow routing in directions governed by surface slope in a mass-conserving manner, as used to compute 'balance velocities'[29,1] for the ice sheet (velocities that keep its surface at steady state, given an accumulation-rate pattern), offers a tantalizing clue to the mechanisms, because the plot of balance speeds against convergence found from such routing forms a diffused tower, even though its details are incorrect (Supplementary Fig. 6). Pinpointing the mechanisms will require deeper theoretical analysis of three-dimensional ice flow with the convergence data. State-of-the-art simulations[16–19] can aid this enquiry, but it is important to scrutinize how valid are their parameterizations of basal processes for predicting migrating and branching ice streams.

Future research should go beyond tuned numerical simulations to strive for holistic understanding of ice-stream systems, by exploiting tools for studying spatial networks (e.g. ref. 30) and measures beside convergence. Immediate extensions include mapping flow convergence for the Greenland Ice Sheet and smaller ice masses, resolving chaos regions with accurate velocity measurements, and tracking how convergence varies with time.

174 **References**


175 1. Bamber, J. L., Vaughan, D. G. & Joughin, I. Widespread complex flow in the interior
176 of the Antarctic Ice Sheet. *Science* **287**, 1248−1250 (2000).

177 2. Alley, R. B. & Bindschadler, R. A. in *The West Antarctic Ice Sheet: Behavior and*
178 *Environment* (eds Alley, R. B. & Bindschadler, R. A.) Antarctic Research Series
179 **77**, 1−11 (American Geophysical Union, Washington DC, 2001).

180 3. Bennett, M. R. Ice streams as the arteries of an ice sheet: their mechanics, stability
181 and significance. *Earth-Sci. Rev.* **61**, 309−339 (2003).

182 4. Hulbe, C. & Fahnestock, M. Century-scale discharge stagnation and reactivation of
183 the Ross ice streams, West Antarctica. *J. Geophys. Res.* **112**, F03S27 (2007).

184 5. Joughin, I. & Alley, R. B. Stability of the West Antarctic ice sheet in a warming
185 world. *Nature Geosci.* **4**, 506−513 (2011).

186 6. Rignot, E., Mouginot, J. & Scheuchl, B. Ice flow of the Antarctic Ice Sheet. *Science*
187 **333**, 1427−1430 (2011).

188 7. Glasser, N. F. & Gudmundsson, G. H. Longitudinal surface stuctures (flowstripes) on
189 Antarctic glaciers. *Cryosphere* **6**, 383−391, doi:10.5194/tc-6-383-2012 (2012).

190 8. Stokes, C. R. & Clark, C. D. Palaeo-ice streams. *Quat. Sci. Rev.* **20,** 1437−1457
191 (2001).

192 9. King, E. C., Woodward, J. & Smith, A. M. Seismic and radar observations of
193 subglacial bed forms beneath the onset zone of Rutford Ice Stream, Antarctica. *J.*
194 *Glaciol.* **53**, 665−672 (2007).

195 10. Alley, R. B., Blankenship, D. D., Bentley, C. R. & Rooney, S. T. Deformation of till
196 beneath ice stream B, West Antarctica. *Nature* **322**, 57−59 (1986).

11. Anandakrishnan, S., Blankenship, D. D., Alley, R. B. & Stoffa, P. L. Influence of subglacial geology on the position of a West Antarctic ice stream from seismic observations. *Nature* **394**, 62−65 (1998).

12. Raymond, C. F., Catania, G. A., Nereson, N. & Van der Veen, C. J. Bed radar reflectivity across the north margin of Whillans Ice Stream, West Antarctica, and implications for margin processes. *J. Glaciol.* **52**, 3−10 (2006).

13. Ng, F. & Conway, H. Fast-flow signature in the stagnated Kamb Ice Stream, West Antarctica. *Geology* **32**, 481−484 (2004).

14. Kamb, B. in *The West Antarctic Ice Sheet: Behavior and Environment* (eds Alley, R. B. & Bindschadler, R. A.) Antarctic Research Series **77**, 157−199 (American Geophysical Union, Washington DC, 2001).

15. Raymond, C. F. Energy balance of ice streams. *J. Glaciol.* **46**, 665−674 (2000).

16. Sayag, R. & Tziperman, E. Interaction and variability of ice streams under a triple-valued sliding law and non-Newtonian rheology. *J. Geophys. Res.* **116**, F01009 (2011).

17. Kyrke-Smith, T. M., Katz, R. F. & Fowler, A. C. Subglacial hydrology and the formation of ice streams. *Proc. R. Soc.* **A470**, 20130494 (2013).

18. Kleiner, T. & Humbert, A. Numerical simulations of major ice streams in western Dronning Maud Land, Antarctica, under wet and dry basal conditions. *J. Glaciol.* **60**, 215−232 (2014).

19. Joughin, I., Smith, B. E. & Medley, B. Marine ice sheet collapse potentially under way for the Thwaites Glacier Basin, West Antarctica. *Science* **344**, 735−738 (2014).

20. Robel, A. A., DeGiuli, E., Schoof, C. & Tziperman, E. Dynamics of ice stream temporal variability: Modes, scales, and hysteresis. *J. Geophys. Res.* **F118**, 925−936 (2013).

21. Schoof, C. Thermally driven migration of ice-stream shear margins. *J. Fluid Mech.* **712**, 552−578 (2012).

22. Bingham, R. G. *et al.* Inland thinning of West Antarctic Ice Sheet steered along subglacial rifts. *Nature* **487**, 468−471 (2012).

23. Nye, J. F. A topological approach to the strain-rate pattern of ice sheets. *J. Glaciol.* **39**, 10−14 (1993).

24. Fretwell, P. *et al*. BEDMAP2: improved ice bed, surface, and thickness datasets for Antarctica. *Cryosphere* **7**, 375−393, doi:10.5194/tc-7-375-2013 (2013).

25. Gudmundsson, G. H. Transmission of basal variability to a glacier surface. *J. Geophys. Res.* **108**(B5), 2253 (2003).

26. Hulbe, C. L. and Whillans, I. M. Weak bands within Ice Stream B, West Antarctica. *J. Glaciol.* **43**, 377−386 (1997).

27. Stokes, C. R., Clark, C. D., Lian, O. B. & Tulaczyk, S. Ice stream sticky spots: A review of their identification and influence beneath contemporary and palaeo-ice streams. *Earth-Sci. Rev.* **81**, 217−249 (2007).

28. Sergienko, O. V. & Hindmarsh, R. C. A. Regular patterns in frictional resistance of ice-stream beds seen by surface data inversion. *Science* **342**, 1086−1089 (2013).

29. Budd, W. F. & Warner, R. C. A computer scheme for rapid calculations of balance-flux distributions. *Ann. Glaciol.* **23**, 21−27 (1996).

30. Dodds, P. S. & Rothman, D. H. Scaling, universality and geomorphology. *Annu. Rev. Earth Planet. Sci*. **28**, 571−610 (2000).

Correspondence and requests for materials should be addressed to F.S.L.N.

**Acknowledgements:** I thank H. Conway, D.R. MacAyeal and D.J. Jerolmack for their comments on the manuscript and J.L. Bamber for providing balance-velocity data.

**Author contributions:** F.S.L.N. designed the study, computed and analyzed the convergence map, and wrote the paper.

**Additional information:** Methods and Supplementary Information are available in the online version of the paper. Reprints and permissions information is available online at www.nature.com/reprints.

**Competing financial interests:** The author declares no competing financial interests.

**Figure 1. Ice-flow convergence across Antarctica.** Grid resolution is 450 m. **a**, Full map, with drainage basins (i–xviii) and divides. At this scale, streaming texture looks bright, and the intricate chaos texture dark. Colour scale applies to all panels and is optimal for rendering features within streaming texture. **b-f**, Sub-areas sampling the interior, ice-stream networks and ice shelves. Ice-stream/glacier names and speed contours at 20 m $a^{-1}$ (thin) and 200 m $a^{-1}$ (thick curve) are given. Dashed ellipses mark convergence ripples associated with bumps/steps in BEDMAP2 topography[24]; these often pair together to show divergence followed by convergence along flow.

**Figure 2. Convergence pattern in an area of Bindschadler Ice Stream overlying bumpy bed**. See Fig. 1f for location. **a,** BEDMAP2 bed topography[24], surface velocity vectors[6] and speed contours at 20 m $a^{-1}$ and 200 m $a^{-1}$. **b,** Kriged convergence and unit vectors of kriged flow direction. Prominent convergence ripples descending across the plot's central part are caused by subglacial peaks at (-648,-690) and (-659,-667). The plot's top and central parts respectively illustrate chaos and streaming convergence textures.

**Figure 3. Convergence, speed, and cross-flow strain rate distributions. a**, $U$ versus $C$. **b**, $U$ versus $UC$ (points, lower scale) and versus half-peak strain rates $UC_+$ and $UC_–$ (curves, upper scale). See **d** for definitions of $C_+$ and $C_–$. **c**, Half-peak convergence $C_+$ and $C_–$ of histograms of $C$ at different speeds; $C_–$ reflected into $C > 0$ (dashed curve) highlights excess $C_+$ at intermediate speeds. **d**, Unit-area histogram of $C$ at $U$ = 100 m $a^{-1}$. As at other speeds, the distribution is non-Gaussian and resembles the Laplace distribution. **e**, $U$ versus $C$ for individual drainage basins in Fig. 1a.

## Methods

### Definition of convergence *C*.

Ice-flow convergence (or divergence) is mentioned but rarely quantified in glaciology. My definition $C = \partial\theta/\partial n = \mathbf{n}.\nabla\theta$ is purely geometrical (Supplementary Fig. 1a) and involves no forces nor conservation laws. Equivalently, $C$ measures the local curvature of curves orthonormal to flow lines, with its sign positive when the curves are concave towards flow (Supplementary Fig. 1c). The curvature of flow lines is independent of $C$ and does not quantify flow merging/splitting (as said in the text), but may be studied in future work for additional geometric properties of tributarized ice flow.

By considering how fast an ice element shortens laterally as it moves down flow at speed $U$, $C$ can be linked to the cross-flow compressive strain rate (Supplementary Fig. 1b). Define a local coordinate system ($x$, $y$) centred at point P and the local velocity field as ($u$, $v$), with $x$ and $u$ oriented along flow, and $y$ and $v$ across, such that ($u$, $v$) = ($U$, 0) at P, then $C = -(\partial v/\partial y)/U$ there.

For a hypothetical circular ice sheet of constant thickness $h$ spreading radially at steady state, receiving constant accumulation rate $a$ and losing mass by calving only, geometry gives $C = -1/r$ and mass conservation gives $U = ar/2h$ at radius $r$. Eliminating $r$ yields $C = -a/2hU$, as used in the text.

An estimate of $C$ in a vortex above a drain hole of diameter $D$ is, assuming cylindrical symmetry for the flow, $2/D$ (= $5\times10^4$ km$^{-1}$ if $D$ = 4 cm).

### Estimating *C* from surface velocity.

INSAR measurements of Antarctic ice-surface velocity **v** on a 450-m polar stereographic projection ($X$-$Y$) grid[6,31] with secant plane at 71°S were converted to $\theta$

measuring clockwise from the $Y$-axis on the same grid. All of my results pertain to the collection period of these measurements: 1996 to 2011. The projection is conformal. The $\theta$-field inherits noise (measurement errors, artefacts), irregular boundaries (e.g. ice-sheet margin) and data voids from **v**. Convergence $C$ is a gradient estimate of this field. To estimate $C$, I used kriging interpolation[32,33] because this geostatistical approach can handle irregular-spaced input data, and, when yielding estimates, it accounts for spatial autocorrelation of the input data (shown by their variogram) and filters and smoothes them accordingly to extract signals. My method is elaborated below. In contrast, simple finite differencing of the $\theta$-values would yield estimates of $C$ more strongly dominated by noise, and the choice of any subsequent spatial filtering to smooth $C$ would be difficult to justify. One could also find $C$ via the lateral strain rate above, but then kriging is needed several times for estimating (from **v**) both strain-rate components and flow direction; the latter is needed for resolving the strain-rate components across flow.

As in most kriging practices, first the experimental variogram $\gamma(h)$ for all $\theta$-values, where $h$ is separation distance, was compiled (Supplementary Fig. 2; filled circles). In calculating semivariance $\gamma$, mismatch between flow directions is quantified by the squared norm of the difference between their unit vectors to avoid problems with circular statistics[34,35]. $\gamma(h)$ shows that flow directions on the ice sheet are well correlated at $h \lesssim 4$ km (Supplementary Fig. 2; filled circles); this suggested the kriging range used below.

Next, assuming a fitted variogram model (solid curve, Supplementary Fig. 2) and 6 km as the range, Continuous-Part Kriging (CPK)[33] was applied at each grid point to re-estimate $\theta$ from the input data of $\theta$ there and in the neighbourhood. For areas without voids, the interpolation uses > 500 neighbouring grid points. The non-zero nugget $\gamma(0)$ represents uncorrelated noise in $\theta$ due to measurement errors and sub-grid-

343 scale effects. Its use in CPK suppresses noise so that the re-estimated flow direction,
344 $\theta_K(X, Y)$, is a smoothed version of the $\theta$-field and approximates its continuous (signal)
345 part[33]. The fitted variogram model function is designed to be parabolic at $h = 0$ to make
346 $\theta_K$ continuous and differentiable[33,35].

347 The final step computed $C$ at each grid point as the gradient of $\theta_K$ in the
348 direction left-perpendicular to $\theta_K$, by using a method where spatial differentiation is
349 embedded in CPK[36]. The kriging system—the interpolation sum and equations for the
350 kriging weights and for the kriging standard derivation—is detailed in ref. 36. The same
351 variogram model and range as before were used. In both CPK steps, flow directions
352 were treated vectorially, with the interpolation sum evaluated as the Fisher sum[35,37] of
353 direction cosines. The kriging standard deviation (a statistical error estimate for the
354 Fisher sum) was converted to $\sigma_C$, the kriging standard deviation for $C$, by normalizing
355 its size by the sum magnitude. Throughout variogram compilation and kriging, true
356 geodetic distances found by correcting grid distances with the projection scale factor
357 were used.

358 The grid spacing imposes a theoretical maximum limit on the gradient of $\theta$ that
359 two neighbouring grid points can resolve, of $\approx \pi/(450\text{ m})$ or 6.98 $\text{km}^{-1}$. Yet CPK can
360 produce unrealistic values of $|C|$ exceeding this limit because it uses many grid points
361 in optimal estimation. Hence values in the output convergence grid were clipped to
362 within $\pm 6.98\ \text{km}^{-1}$. Clipping occurred in chaos regions only.

363 The flow-speed and convergence data in Supplementary Fig. 6 derive from the
364 Antarctic balance-velocity model of ref. 1 (updated velocities based on newer ice-sheet
365 surface topography[38] after recalculation by J.L. Bamber). Convergence was estimated
366 from flow direction by a kriging procedure like the one above.

367

**Error analysis and robustness of the tower dependence.**

$\theta_K(X, Y)$ was validated by checking that the residuals $\theta_K - \theta$ are unbiased and uncorrelated, and $\sigma_\theta^2$ (kriging variance for $\theta_K$) adequately accounts for their variance in streaming regions. Typically, $\sigma_\theta \approx 5^\circ$ in these regions.

In contrast, kriged estimates of $C$ cannot be validated because independent estimates of $C$ based on direct strain-rate measurements rather than based on only velocity measurements are unavailable. Although the kriging standard deviation $\sigma_C$ at each grid point is known, it does not reflect the local variability of the $C$-field, so it cannot be used to assess how errors in $C$ impact the results in Figure 3 (see further discussion below). Specifically, the kriging standard deviation is a global measure of uncertainty that accounts only for the variogram and the configuration of kriging interpolation grid points (e.g. refs. 32, 33). $\sigma_C$ is near-uniform ($\approx 0.13$ km$^{-1}$) in streaming regions; expectedly, it rises within a few grid spacings of boundaries and data voids and fluctuates strongly in chaos regions, attesting the unreliability of the kriged estimates of $C$ in these areas.

As the text describes, in chaos regions, low flow speeds allow measurement errors in $\mathbf{v}$ to corrupt $\theta$ and obscure these regions' true convergence. To demonstrate this effect, I conducted the experiment in Supplementary Fig. 7 where, in an otherwise parallel flow, deliberate error in $\theta$ was introduced to a grid point, causing a convergence dipole. More errors in the neighbourhood can then produce the random-looking, short-scale convergence-divergence pattern in chaos regions. Comparing $\theta_K$ to $\theta$ in chaos regions confirms that $\theta_K$ has been smoothed to some extent by kriging, but kriging cannot negate such errors to recover convergence reliably. Not surprisingly, weak traces of chaos are visible in some slow parts of streaming regions (Fig. 1); their short length-scale precludes their being mistaken as convergence ripples.

Whether errors in $U$ and $C$ can upset my inference from Figure 3 of the tower-shaped speed dependence of the $C$-distribution needs consideration. Errors in $U$ ($\lesssim$ 17 m $a^{-1}$)[6] are negligible in the large speed range of interest. To derive error estimates for $C$, I use the knowledge that $C$-values in streaming regions portray spatially-coherent features on the convergence map. Whether such feature is a convergence ripple, a curvilinear shear-margin zone, or an area of near-parallel or uniformly converging/diverging flow on an ice stream, a key characteristic of it is that $C$ does not vary much across the feature. This idea motivates the calculation of the mean $\overline{C}$ and standard deviation $\sigma$ of the $C$-values in separate 'block regions' across the ice sheet; $\sigma$ is then an error estimate of $C$ for each block. The tower dependence is assured if some blocks with low $U$ have convergence statistics ($\left|\overline{C}\right| \pm \sigma$) more extreme than the most extreme block convergence/divergence estimates found at higher $U$. The results, in Supplementary Figure 5, confirm these instances and the integrity of the dependence. The block size in this analysis, 25 by 25 grid points, is chosen to be not too large compared to the typical size of the features.

**Removal of spurious data, and sensitivity to choice of variogram model.**

The raw plot of $U$ versus $C$ from my kriging calculation showed outliers from the tower (red points, Supplementary Fig. 4a). Examination of these outliers with the input velocity field **v** showed them to be false 'excursions' caused by: (i) isolated grid points—often on the edge of data voids—where **v** (thus also $U$) is anomalous compared to that in adjacent areas, or (ii) positions one or two grid spacings from ice-free areas (e.g. mountains) or data voids where kriging uncertainty ($\sigma_C$) becomes high and $C$ is anomalous compared to $C$ in adjacent areas. Fig. 3a is the processed plot after results

from these places and from all grid points within two grid spacings of boundaries and voids have been excluded. The same processing preceded the making of Figs 3b–e.

Finally, my kriging procedure can be criticized for assuming a best-fit variogram model for the whole ice sheet (including chaos regions), when ultimately, the $C$-values in chaos regions are deemed unusable and excluded from analysis. To show that the paper's conclusions are not hinged on this assumption, I repeated the kriging to compute $C$ in streaming regions, this time assuming the best-fit variogram model for regions where $U > 20$ m a$^{-1}$ (dashed curve, Supplementary Fig. 2). The resulting convergence map looks practically the same as Figure 1 except it is less smoothed and conveys more spatial details/noise, notably in slower areas of streaming regions. This is expected because the new model $\gamma$, which is an average estimate for the speed range $U > 20$ m a$^{-1}$, underestimates $\gamma$ for ice flow at the lower end of this range. Crucially, while rekriging changed all convergence estimates numerically, all essential mapped features (e.g. ripples) discussed in the text remain valid, and remaking of Figs 3a,c,d shows negligible change in both the $C$-distribution and its speed dependence (Supplementary Figs 4b–d).

**Data availability.** Gridded data of the Antarctic Ice Sheet's flow convergence and cross-flow strain rate are archived at http://doi.pangaea.de/10.1594/PANGAEA.841137.

**Code availability.** The code used to compute the variogram of flow direction and the convergence values is available on request from Felix Ng (f.ng@sheffield.ac.uk).

## References for the Methods


31. Rignot, E., Mouginot, J. & Scheuchl, B. *MEaSUREs InSAR-Based Antarctica Ice Velocity Map*. Boulder, Colorado USA: NASA DAAC at the National Snow and Ice Data Center. http://dx.doi.org/10.5067/MEASURES/CRYOSPHERE/nsidc-0484.001 (2011).

32. Isaaks, E. H. & Srivastava, R. M. *Applied Geostatistics* (Oxford Univ. Press, New York, 1989).

33. Kitanidis, P. K. *Introduction to Geostatistics: Applications in Hydrogeology* (Cambridge Univ. Press, Cambridge, 1997).

34. Young, D. S. Random vectors and spatial analysis by geostatistics for geotechnical applications. *Math. Geol.* **19**, 467−479 (1987).

35. Gumiaux, C., Gapais, D. & Brun, J. P. Geostatistics applied to best-fit interpolation of orientation data. *Tectonophysics* **376**, 241−259 (2003).

36. Philip, R. D. & Kitanidis, P. K. Geostatistical estimation of hydraulic head gradients. *Ground Water* **27**, 855−865 (1989).

37. Fisher, N. I. *Statistical Analysis of Circular Data* (Cambridge Univ. Press, Cambridge, 1993).

38. Bamber, J. L., Gomez-Dans, J. L. & Griggs, J. A. A new 1 km digital elevation model of the Antarctic derived from combined satellite radar and laser data – Part 1: Data and methods. *Cryosphere* **3**, 101−111, doi:10.5194/tc-3-101-2009 (2009).

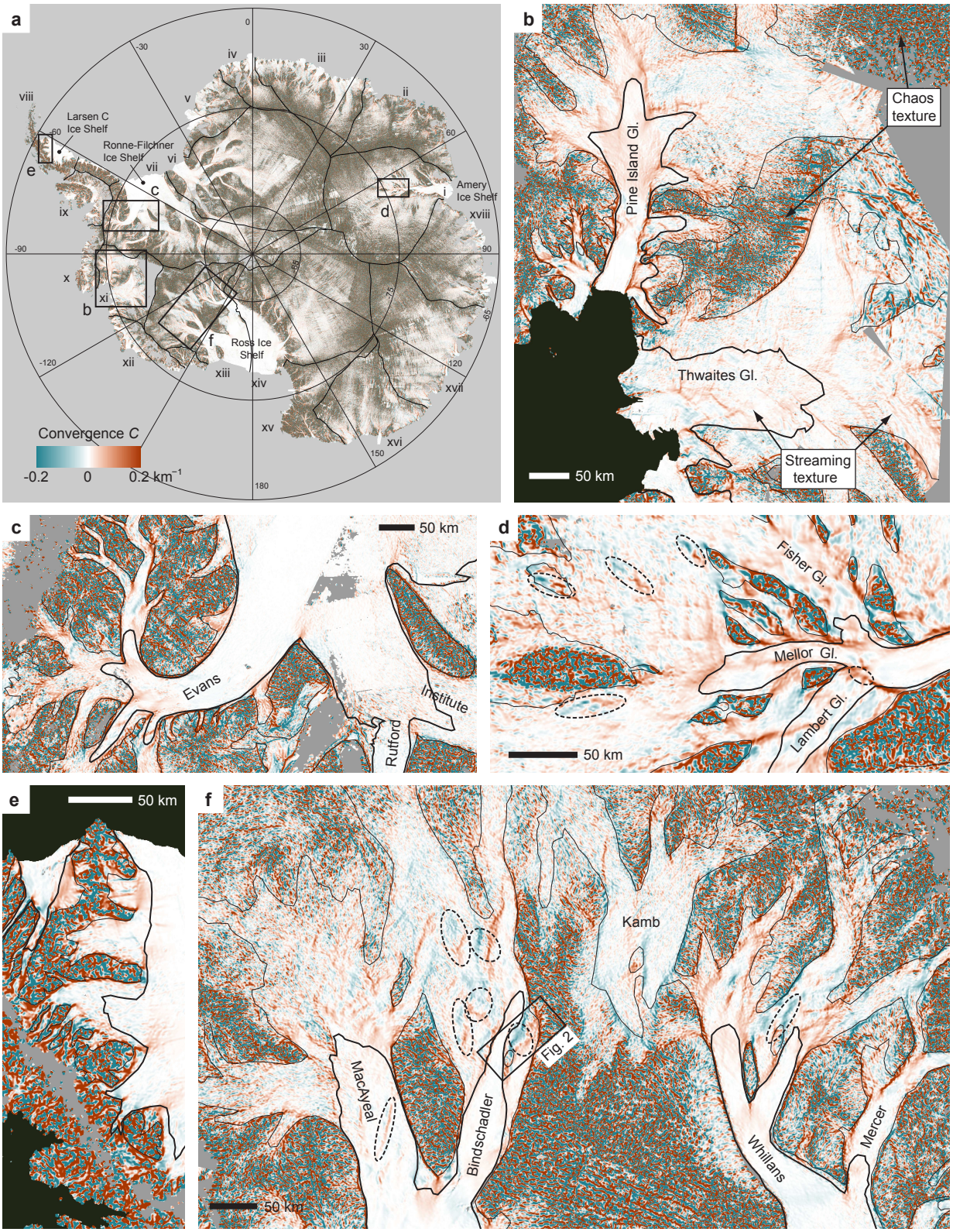
a
Larsen C Ice Shelf
Ronne-Filchner Ice Shelf
Amery Ice Shelf
Ross Ice Shelf
Convergence C
-0.2
0
0.2 km$^{-1}$
b
Chaos texture
Pine Island Gl.
Thwaites Gl.
Streaming texture
50 km
c
Evans
Institute
Rutford
50 km
d
Fisher Gl.
Mellor Gl.
Lambert Gl.
50 km
e
50 km
f
Kamb
MacAyeal
Bindschadler
Whillans
Mercer
Fig. 2
50 km

Figure 1

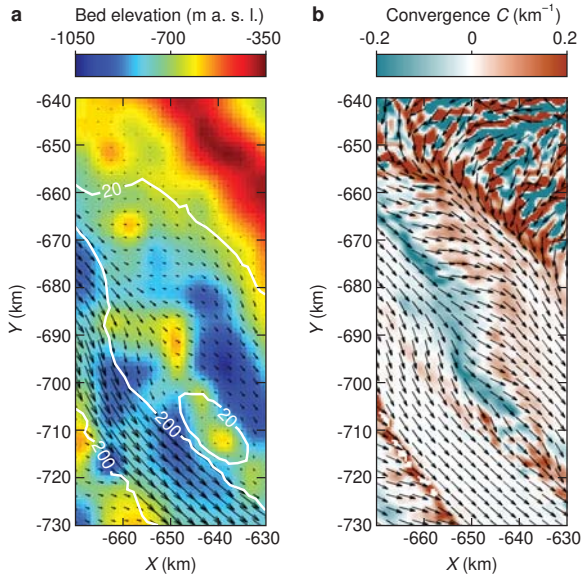
a
Bed elevation (m a. s. l.)
-1050
-700
-350
b
Convergence C (km−1)
-0.2
0
0.2
-640
-650
-660
-670
-680
-690
-700
-710
-720
-730
Y (km)
20
200
200
20
-660
-650
-640
-630
X (km)

Figure 2

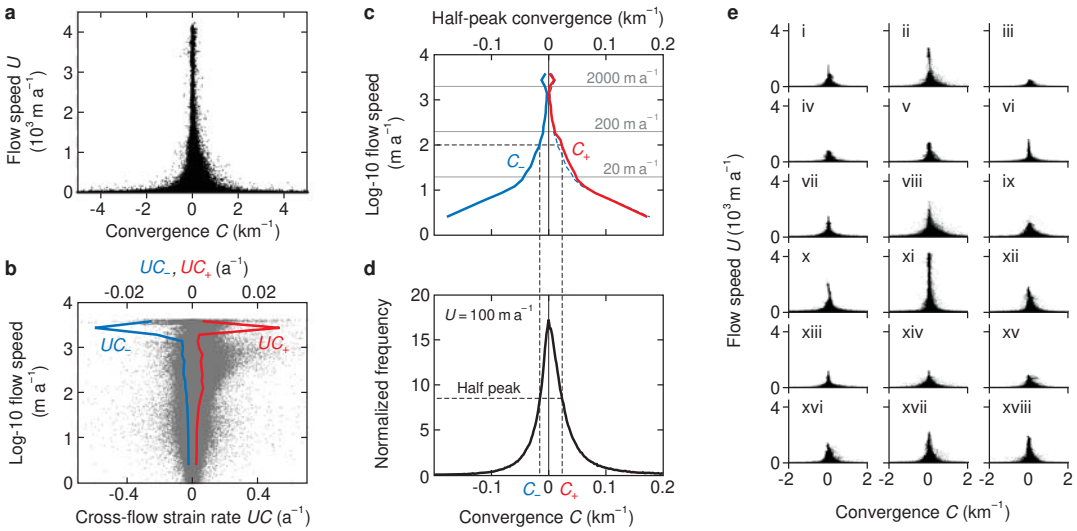
a
Flow speed U (10^3 m a^-1)
Convergence C (km^-1)
b
UC_-, UC_+ (a^-1)
Log-10 flow speed (m a^-1)
Cross-flow strain rate UC (a^-1)
c
Half-peak convergence (km^-1)
Log-10 flow speed (m a^-1)
2000 m a^-1
200 m a^-1
20 m a^-1
C_-
C_+
d
Normalized frequency
U = 100 m a^-1
Half peak
Convergence C (km^-1)
e
i
ii
iii
iv
v
vi
vii
viii
ix
x
xi
xii
xiii
xiv
xv
xvi
xvii
xviii
Flow speed U (10^3 m a^-1)
Convergence C (km^-1)

Figure 3

**Supplementary Information for the paper 'Spatial complexity of ice flow across the Antarctic Ice Sheet' by Felix S. L. Ng**

This file contains Supplementary Figures 1 to 7 and their captions.

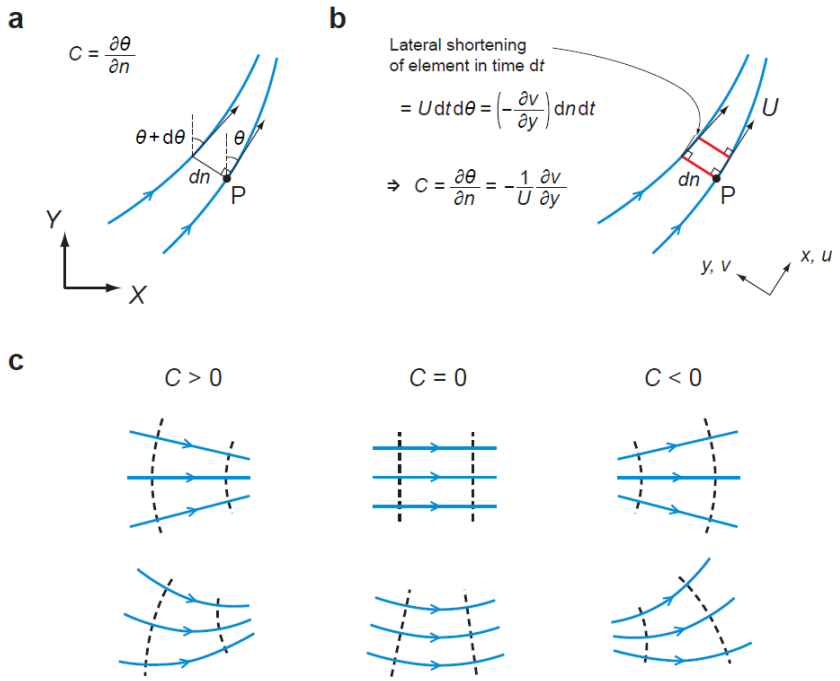


**Supplementary Figure 1. Definition of convergence *C* for planimetric flow fields. a**, $C$ as the local rate of change of flow direction $\theta$ across flow. **b**, Relation between $C$, flow speed $U$ and lateral strain rate $-\partial v/\partial y$. **c**, The signs of $C$ for archetypal flow fields. Dashed lines are curves orthonormal to flow lines.

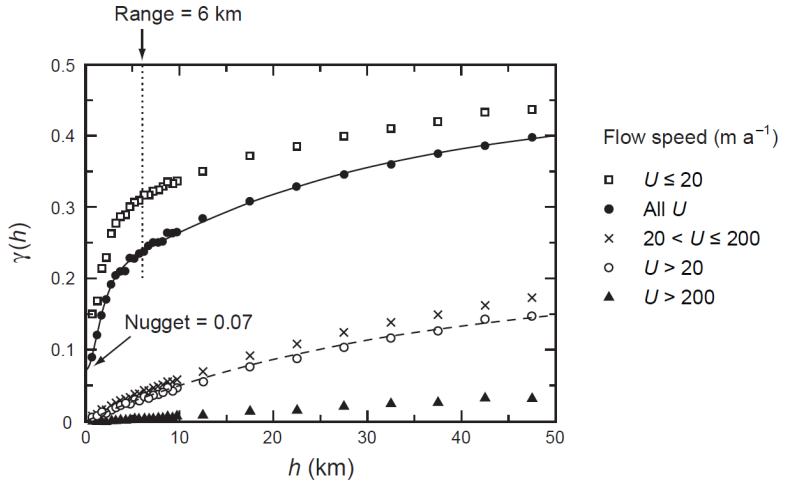


**Supplementary Figure 2. Vectorial variogram for ice-flow directions on the Antarctic Ice Sheet.** Following ref. 34, empirical variogram data (symbols) for flow in different speed ranges were calculated by $\gamma(h) = \Sigma \left| \boldsymbol{z}(X,Y) - \boldsymbol{z}(X+\mathrm{d}X, Y+\mathrm{d}Y) \right|^2/(2N(h))$, where $\gamma$ is semivariance, $\boldsymbol{z}$ is unit vector representing flow direction $\theta$, $h$ is geodetic distance between each pair of positions ($X$, $Y$) and ($X+\mathrm{d}X$, $Y+\mathrm{d}Y$), and summation is done over all non-repeating position pairs ($N$ being their total number) falling in different bins of $h$. Semivariance decreases with speed at all distances. Steep slope of $\gamma(h)$ near the origin at low speeds indicates spatial non-smoothness of $\theta$ in chaos regions; its low slope at high speeds indicates smoothness of $\theta$ in streaming regions. Solid curve is the fitted variogram model for the whole ice sheet: $\gamma = A_0 + A_1(1 - \exp(-((h^2+A_5^2)^{0.5}-A_5)/A_2)) + A_3(1 - \exp(-((h^2+A_5^2)^{0.5}-A_5)/A_4))$, with parameters $A_0$ = 0.07 (nugget), $A_1$ = 0.133, $A_2$ = 0.85, $A_3$ = 0.24, $A_4$ = 28, $A_5$ = 2. Dashed curve is the fitted variogram model for regions where $U > 20$ m a$^{-1}$ (thus, streaming regions mostly): $\gamma = A_0 + A_1(1 - \exp(-((h^2+A_3^2)^{0.5}-A_3)/A_2))$, with $A_0$ = 0.002 (nugget), $A_1$ = 0.188, $A_2$ = 33, $A_3$ = 0.3.

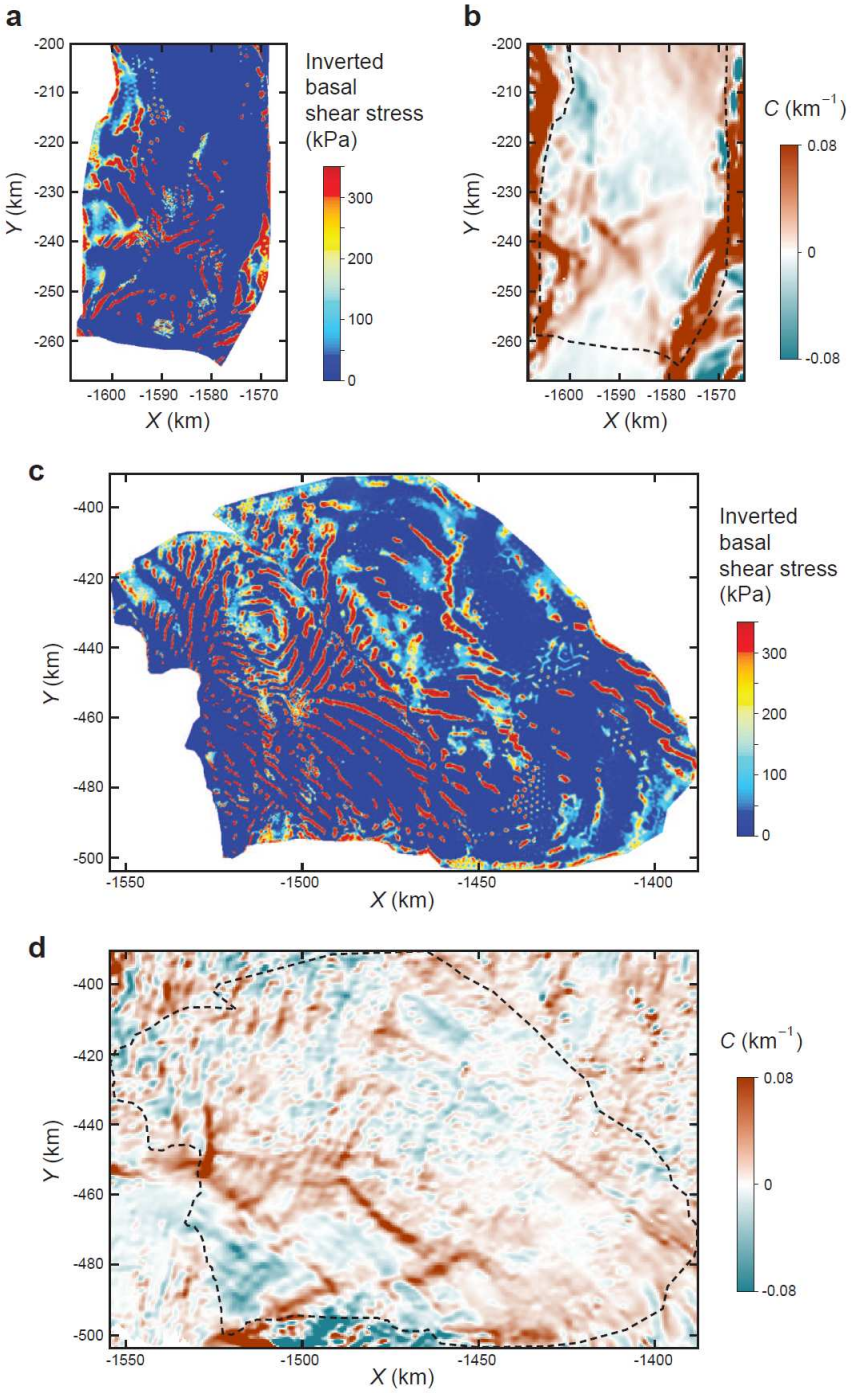


28

29 **Supplementary Figure 3. Flow convergence and basal shear stress on the trunk**
30 **regions of Pine Island Glacier (a,b) and Thwaites Glacier (c,d).** The region on each
31 glacier is near the central part of the area enclosed by the 200 m $a^{-1}$ contour in Fig. 1b.
32 **a,c,** Modelled basal shear stress. Both panels are reproduced from ref. 28 with
33 permission from AAAS. **b,d,** Convergence *C* from the present study. Basal shear stress

and $C$ describe different aspects of the ice motion so their patterns are expected to differ, but some correlation between them is notable. In **c** and **d**, many convergence ripples and 'rib areas' of high stress (red) have similar positions, spacing and orientation. In **a** and **b**, this is exemplified by the cross-like features near (-1590,-240). Also, for both glaciers, areas exhibiting high-amplitude spatial variations in $C$ tend to have more ribs.

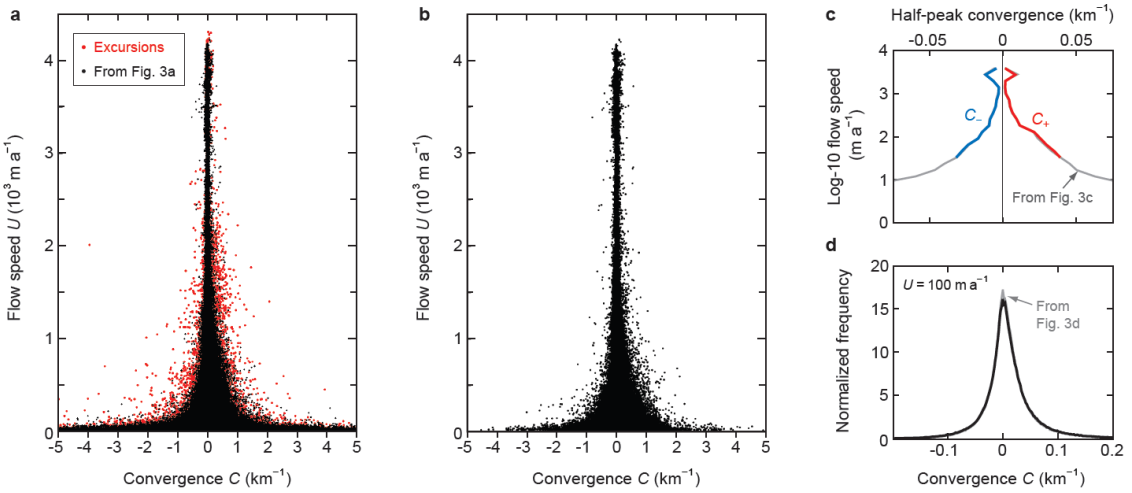


**Supplementary Figure 4. Robustness of kriged estimates of flow convergence. a**, Scatter plot in Fig. 3a (black points) and false excursions (red) resulting from spurious input data and edge effects of boundaries and data voids. **b**, $U$ against $C$ for regions where $U > 20$ m a$^{-1}$ (thus mostly streaming regions), recomputed by kriging with the variogram model specific for these regions (dashed curve in Supplementary Fig. 2). **c**, Dependence of half-peak convergence $C_+$ and $C_-$ on flow speed for the results in **b**. **d**, Unit-area histogram of $C$ at $U = 100$ m a$^{-1}$ for the results in **b**. Comparison of panels **b**–**d** with Figs 3a,c,d shows that rekriging hardly changes the $C$-value distribution.

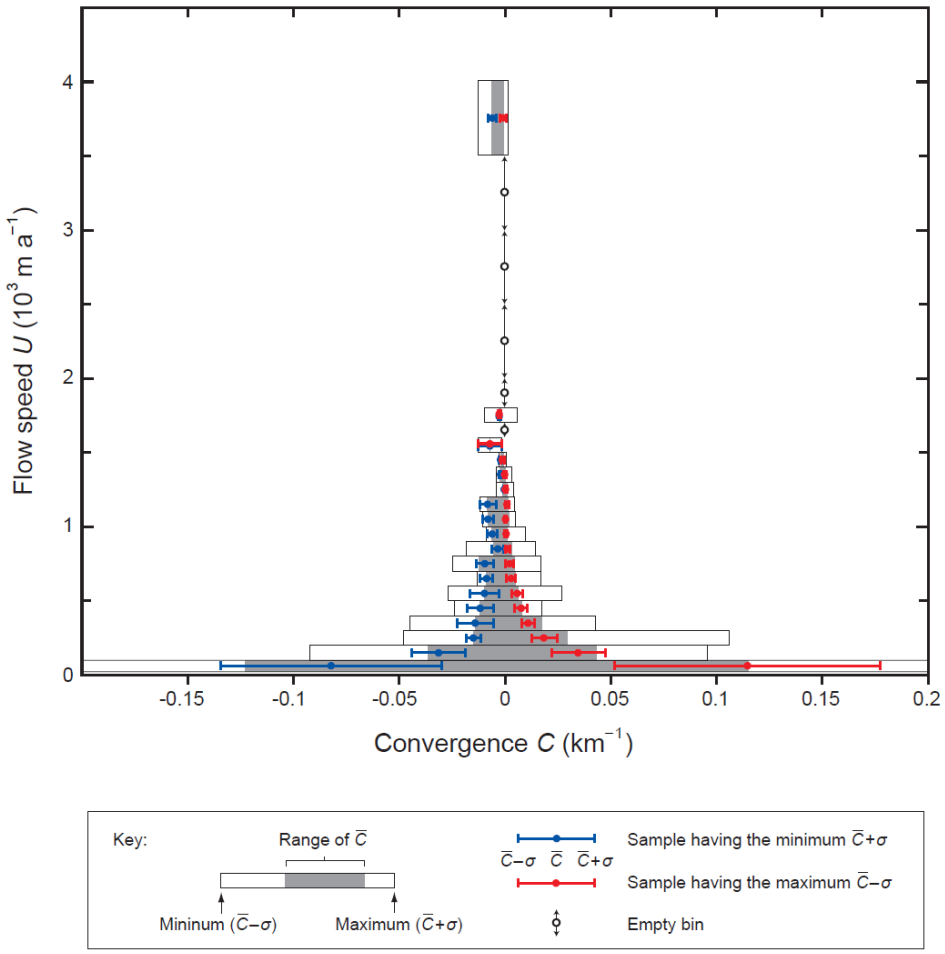


51

52 **Supplementary Figure 5. Binned analysis of convergence and its errors for**
53 **contiguous block regions across the ice sheet.** A block, measuring 25 grid points on a
54 side, is sampled if it has ≤ 10% void pixels and its speed range falls entirely within a
55 speed bin. $\bar{C}$ denotes the mean of *C*-values in the block, and $\sigma$ their standard deviation.
56 In the figure, each bin gathers blocks with similar speeds *U*; grey bar indicates the range
57 of $\bar{C}$; white box indicates the expanded range from minimum $\bar{C}-\sigma$ to maximum $\bar{C}+\sigma$.
58 Two sets of 'dot and whiskers' plot $\bar{C}$ and $\bar{C}\pm\sigma$ of the sample whose $\bar{C}+\sigma$ is the least
59 (blue), and of the sample whose $\bar{C}-\sigma$ is the greatest (red). That such samples in some
60 lower-speed bins lie outside the expanded range of some higher-speed bins confirms
61 that kriging uncertainty in *C* cannot nullify its 'tower dependence' on *U*.

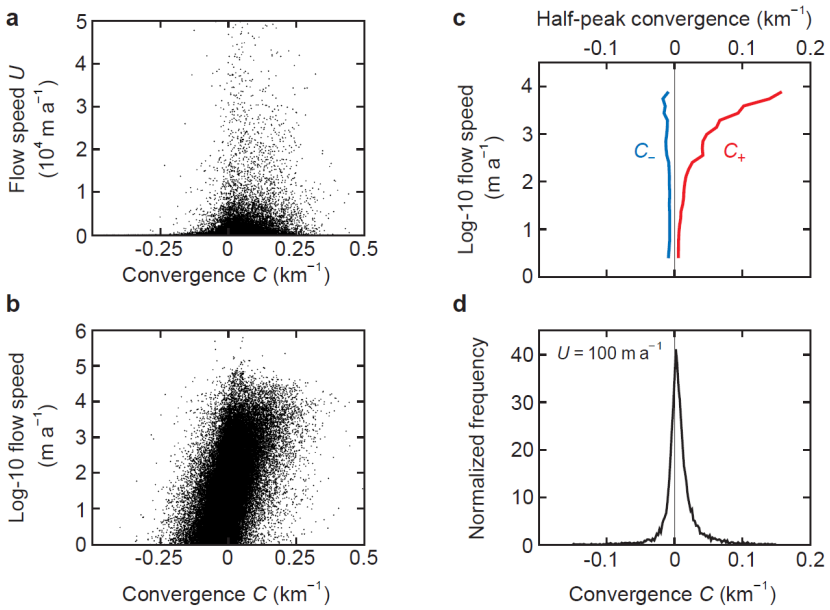


62

63

64 **Supplementary Figure 6. Ice-flow convergence and speed from the ice sheet's**
65 **balance-velocity field computed by ref. 1. a**, Scatter plot of $U$ versus $C$, showing a
66 tower shape less well defined than the one in Fig. 3a. **b**, The same scatter plot in log-10
67 speed scale, revealing a deficiency of convergent flow at speeds $\lesssim 10^3$ m a$^{-1}$. **c**, Half-
68 peak convergence $C_+$ and $C_-$ of histograms of $C$ at different speeds. **d**, Unit-area
69 histogram of $C$ at $U = 100$ m a$^{-1}$.

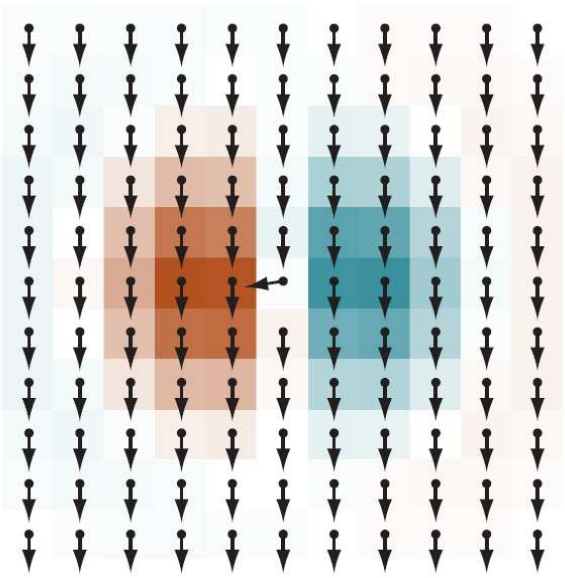

**Supplementary Figure 7. Dipole convergence pattern in a kriging experiment.** Error in flow direction is imposed at one grid point of an otherwise parallel flow field to simulate how errors in INSAR-measured velocity can cause the convergence pattern in chaos regions. Arrows signify unit vectors of input flow-direction data. The colour scale for convergence is the same as in Fig. 1.